Received: 6 February 2020 | Revised: 14 August 2020 | Accepted: 14 August 2020

DOI: 10.1002/mrm.28507

FULL PAPER

Magnetic Resonance in Medicine

Separation of fluid and solid shear wave fields and quantification of coupling density by magnetic resonance poroelastography

Ledia Lilaj[1] | **Thomas Fischer**[2] | **Jing Guo**[1] | **Jürgen Braun**[3] | **Ingolf Sack**[1] | **Sebastian Hirsch**[4,5]

[1]Department of Radiology, Charité – Universitätsmedizin Berlin, Berlin, Germany

[2]Department of Radiology, Interdisciplinary Ultrasound Center, Charité – Universitätsmedizin Berlin, Berlin, Germany

[3]Institute of Medical Informatics, Charité – Universitätsmedizin Berlin, Berlin, Germany

[4]Berlin Center for Advanced Neuroimaging, Charité – Universitätsmedizin Berlin, Berlin, Germany

[5]Bernstein Center for Computational Neuroscience, Berlin, Germany

Correspondence
Sebastian Hirsch, Berlin Center for Advanced Neuroimaging, Charité – Universitätsmedizin Berlin, Charitéplatz 1, Berlin 10117, Germany.
Email: sebastian.hirsch@charite.de

Funding information
Deutsche Forschungsgemeinschaft, Grant/Award Number: BIOQIC GRK2260, and Matrix in Vision SFB1340

Purpose: Biological soft tissues often have a porous architecture comprising fluid and solid compartments. Upon displacement through physiological or externally induced motion, the relative motion of these compartments depends on poroelastic parameters, such as coupling density (ρ_{12}) and tissue porosity. This study introduces inversion recovery MR elastography (IR-MRE) (1) to quantify porosity defined as fluid volume over total volume, (2) to separate externally induced shear strain fields of fluid and solid compartments, and (3) to quantify coupling density assuming a biphasic behavior of in vivo brain tissue.

Theory and Methods: Porosity was measured in eight tofu phantoms and gray matter (GM) and white matter (WM) of 21 healthy volunteers. Porosity of tofu was compared to values obtained by fluid draining and microscopy. Solid and fluid shear-strain amplitudes and ρ_{12} were estimated both in phantoms and in in vivo brain.

Results: T_1-based measurement of tofu porosity agreed well with reference values ($R = 0.99$, $P < .01$). Brain tissue porosity was 0.14 ± 0.02 in GM and 0.05 ± 0.01 in WM ($P < .001$). Fluid shear strain was found to be phase-locked with solid shear strain but had lower amplitudes in both tofu phantoms and brain tissue ($P < .05$). In accordance with theory, tofu and brain ρ_{12} were negative.

Conclusion: IR-MRE allowed for the first time separation of shear strain fields of solid and fluid compartments for measuring coupling density according to the biphasic theory of poroelasticity. Thus, IR-MRE opens horizons for poroelastography-derived imaging markers that can be used in basic research and diagnostic applications.

KEYWORDS
brain tissue, coupling density, elastography, inversion recovery, phantom, porosity

1 | INTRODUCTION

MR elastography (MRE) is a noninvasive imaging technique that allows in vivo quantification of the viscoelastic properties of biological soft tissues.[1] In MRE, tissues are usually modeled as monophasic viscoelastic media. However, it has been demonstrated that the mechanical behavior of several tissues, such as brain,[2,3] cartilage,[4,5] or edematous tissue,[6] is better described by a poroelastic model comprising a solid matrix saturated with an incompressible fluid.[7] The solid matrix consists of cells and the extracellular matrix, while the fluid compartment includes interstitial fluid, blood, or cerebrospinal fluid (CSF). The more complex nature of the poroelastic model compared to the monophasic viscoelastic model, including interactions between the compartments, and coupling of motion fields, requires specialized acquisition and postprocessing strategies to exploit the advantages provided by the poroelastic model. To account for the number of unknown model parameters in the poroelastic equations of motion, previous studies have used a priori assumptions about tissue structure.[8] In particular, porosity has never been quantified noninvasively in in vivo brain tissue before. Instead, a global value of, for example, 0.20 for the entire brain, has been assumed.[4,8] In this study, we propose a technique to quantify porosity along with other poroelastic model parameters from a series of measurements. Our motivation is twofold: using spatially resolved maps of the porosity is expected to provide more accurate estimates for the poroelastic parameters than using a global value; and porosity might present itself as a meaningful biomarker to be explored in future studies. While previous applications of poro-MRE have mainly focused on investigating the compression properties of biological tissues,[9,10] in this work, we will concentrate on shear waves since they provide higher SNR than compression waves. The Biot model for poroelastic wave propagation predicts 1 shear wave mode as opposed to 2 compression wave modes.[11]

Our proposed method for poroelastic MRE consists of 4 steps: (1) acquisition of a relaxation curve using inversion recovery (IR-MRI); (2) estimation of porosity and signal parameters of the 2 compartments using a biphasic, biexponential relaxation model; (3) acquisition of MRE data with added IR at two different inversion times (TIs) (IR-MRE); (4) separation of the solid and fluid shear wave fields based on a biphasic MRE signal model.

The general feasibility of this method will be demonstrated using tissue-mimicking phantoms made of coagulated soybean curd (tofu), whose microstructure is characterized by abundant fluid-filled pores.[12] Separating the shear wave fields corresponding to fluid and solid tissue motion will allow us to estimate a new parameter in poroelasticity imaging, namely *coupling density*, ρ_{12}. This parameter is associated with the transfer of kinetic energy between the 2 compartments and is predicted to be negative due to the inability of the fluid to support shear waves.[13]

As an outlook, we will quantify in vivo tissue porosity of the brain considering brain tissue as a porous medium permeated by an extracellular fluid[14] with T_1 relaxation properties similar to CSF.[15] From fluid and solid tissue motions, we will finally quantify ρ_{12} of the the in vivo human brain.

2 | THEORY

Longitudinal relaxation time, T_1, can be mapped using an IR sequence with different TIs and fitting the signal intensity of each voxel with a monoexponential relaxation curve

$$I(TI) = I_\infty \cdot \left(1 - 2 \cdot e^{-\frac{TI}{T_1}}\right) + C. \quad (1)$$

$I(TI)$ is the voxel intensity measured in the image with inversion time TI. I_∞ is the intensity without inversion. C is the noise offset, which is typically two orders of magnitude smaller than I. Since we ensured that $TR > 5 \cdot T_1$ in all measurements, we assumed that each scan was performed with fully relaxed longitudinal magnetization and, therefore, neglected TR-dependent terms in Equation (1).

Most tissue types are not entirely homogeneous across a voxel; they rather have a complex multiphasic structure. In this work, we assume a porous biphasic medium, consisting of a porous solid matrix and a liquid saturating the pore space, with different T_1 constants. The solid compartment is composed of macromolecules and cells, whereas the fluid compartment comprises moving fluids, such as blood, CSF, or interstitial fluid.

2.1 | Porosity estimation by IR-MRI

Porosity f of a porous medium is defined as the volume fraction of the medium that is occupied by the fluid compartment:

$$f = \frac{V^f}{V} \quad (2)$$

where V is a volume element of the medium, and V^f is the enclosed fluid volume. The IR-MRI signal of a biphasic medium is a superposition of the contribution of the 2 compartments, each weighted by its volume fraction: f for the fluid and (1-f) for the solid.

To account for biphasic T_1 signal relaxation, signal intensity is expressed as a function of *TI:*

$$I^m(TI) = I^f \cdot f\left(1-2e^{-\frac{TI}{T_1^f}}\right) + I^s \cdot (1-f)\left(1-2e^{-\frac{TI}{T_1^s}}\right) + C. \quad (3)$$

The superscript m on the left-hand side indicates that this is the measured signal intensity, as opposed to I^s and I^f (the hypothetical signal intensities of the pure solid and fluid material), which can only be quantified indirectly. I^s and I^f also account for the signal intensity dependence on T_2/T_2^* and TE, which are not relevant for this work. In order to estimate porosity, Equation (3) is fitted to a series of IR-MRI scans acquired with different TIs. However, the number of unknown parameters (I^f, I^s, T_1^f, T_1^s, f, C) renders this fitting process unstable. Therefore, we will assess the fluid properties, I^f and T_1^f, in an independent estimation, assuming that their variability across the biphasic object is negligible, thus reducing the unknown parameters to the set (I^s, T_1^s, f, C).

To further simplify the fitting procedure, we focus on the specific case of a scan without inversion pulse (formally, this is identical to $TI \to \infty$, but we will drop the TI dependence in the following formulas)

$$I^{m,\infty} = I^f \cdot f + I^s \cdot (1-f) + C. \quad (4)$$

Since offset C in Equation (4) is typically 2 orders of magnitude lower than I^f and $I^{m,\infty}$, it will be neglected henceforth, improving fitting stability at the expense of precision.

Solving Equation (4) for I^s and substituting into Equation (3) yields the following simplified equation:

$$I^m(TI) = -2 \cdot f \cdot I^f e^{-\frac{TI}{T_1^f}} - 2\left(I^{m,\infty} - f \cdot I^f\right) \cdot e^{-\frac{TI}{T_1^s}} + C. \quad (5)$$

With I^s thusly eliminated as an unknown parameter, the set of fitting parameters is further reduced to f, T_1^s, and offset C.

The IR-MRE signal equation of a biphasic medium is an extension of Equation (3), which includes the motion-induced signal phase:

$$M^m \cdot e^{i\varphi^m} = I^f \cdot f\left(1-2e^{-\frac{TI}{T_1^f}}\right) \cdot e^{i\varphi^f} + I^s(1-f)\left(1-2e^{-\frac{TI}{T_1^s}}\right) \cdot e^{i\varphi^s}. \quad (6)$$

M^m and φ^m represent the magnitude and phase of the measured MRE signal. Equation (6) can be used to decompose the measured compound displacement field, φ^m, into the compartmental fields φ^s and φ^f, if MRE is performed twice with different TIs, denoted TI_1 and TI_2. In the simplest case, we choose $TI_1 \to \infty$ (i.e., no inversion is performed) and $TI_2 = \ln(2) \cdot T_1^f$, that is, the TI that nulls the signal of the fluid. The system of the two versions of Equation (6) for 2 TIs can be solved for φ^s and φ^f

$$e^{i\varphi^s} = \frac{M^{m,2} \cdot e^{i\varphi^{m,2}}}{I^s \cdot (1-f)\left(1-2e^{-\frac{TI^{m,2}}{T_1^s}}\right)} \quad (7)$$

$$e^{i\varphi^f} = \frac{M^{m,1} \cdot e^{i\varphi^{m,1}} - \frac{M^{m,2} \cdot e^{i\varphi^{m,2}}}{\left(1-2e^{-\frac{TI^{m,2}}{T_1^s}}\right)}}{I^f \cdot f} \quad (8)$$

where indices 1 and 2 refer to measurements with TI_1 and TI_2. The displacements φ^s and φ^m can then be extracted by taking the complex phase of the two equations.

2.2 | Biphasic elastic motion

The poroelastic relationship between deformation (strain ε) and the resulting stresses (σ) can be expressed using Biot's law of stress and strain in a biphasic material.[7] We extended this equation to fulfill the condition of single-phase stresses if $f \to 0$ and $\to 1$, as proposed by Sack and Schaeffter[13]:

$$\begin{pmatrix} (1-f)\sigma_{11}^s \\ (1-f)\sigma_{22}^s \\ (1-f)\sigma_{33}^s \\ (1-f)\sigma_{12}^s \\ (1-f)\sigma_{23}^s \\ (1-f)\sigma_{13}^s \\ f\sigma^f \end{pmatrix} = (1-f) \begin{pmatrix} \left(K^s + \frac{4}{3}\mu^s\right) & \left(K^s - \frac{2}{3}\mu^s\right) & \left(K^s - \frac{2}{3}\mu^s\right) & 0 & 0 & 0 & fH \\ \left(K^s - \frac{2}{3}\mu^s\right) & \left(K^s + \frac{4}{3}\mu^s\right) & \left(K^s - \frac{2}{3}\mu^s\right) & 0 & 0 & 0 & fH \\ \left(K^s - \frac{2}{3}\mu^s\right) & \left(K^s - \frac{2}{3}\mu^s\right) & \left(K^s + \frac{4}{3}\mu^s\right) & 0 & 0 & 0 & fH \\ 0 & 0 & 0 & \mu^s & 0 & 0 & 0 \\ 0 & 0 & 0 & 0 & \mu^s & 0 & 0 \\ 0 & 0 & 0 & 0 & 0 & \mu^s & 0 \\ fH & fH & fH & 0 & 0 & 0 & \frac{f}{1-f}K^f \end{pmatrix} \cdot \begin{pmatrix} \varepsilon_{11}^s \\ \varepsilon_{22}^s \\ \varepsilon_{33}^s \\ 2\varepsilon_{12}^s \\ 2\varepsilon_{23}^s \\ 2\varepsilon_{13}^s \\ \varepsilon^f \end{pmatrix}. \quad (9)$$

The displacement of the fluid is expressed by scalar volumetric stress and strain, whereas the full 3D deformation field is required for the solid. K^s and μ^s are the bulk and shear modulus of the solid and K^f is the fluid bulk modulus. The coupling modulus H quantifies the stress induced in one compartment by deformation of the other compartment. Note that this approach, in contrast those by Mcgarry et al and Parker[3,16,17] does not account for additional stresses induced by hydrostatic pressure gradients, since we are only

interested in shear deformation and assume the corresponding model parameters to be pressure-independent. The equations of motion are derived from the balance of momentum,

$$\rho\ddot{\mathbf{u}} = \nabla \cdot \boldsymbol{\sigma} \tag{10}$$

with mass density ρ and displacement field $\mathbf{u}$. Applying the divergence operator to Equation (9), as prescribed by the right-hand side of Equation (10), and separating the resulting equations for solid and fluid motion yields

$$(1-f)\,\nabla \cdot \boldsymbol{\sigma}^s = (1-f)\left[\left(K^s + \frac{1}{3}\mu^s\right)\nabla(\nabla \cdot \mathbf{u}^s) + fH\nabla\varepsilon^f + \mu^s \Delta \mathbf{u}^s\right] \tag{11a}$$

$$f\nabla\sigma^f = f(1-f)H\nabla(\nabla \cdot \mathbf{u}^s) + fK^f\nabla\left(\nabla \cdot \mathbf{u}^f\right). \tag{11b}$$

These equations were derived under the assumption that all elastic properties vary slowly in space, allowing us to neglect their gradients.

Equations (11a and 11b) represent the motion of the full displacement vector field, comprising shear and volumetric deformation. However, from Equation (9), it is obvious that shear strain is decoupled from volumetric stress (and vice versa). Therefore, since elastography usually focuses on shear deformation, and since the shear waves have only one wave mode while the compression waves present two wave modes, we suppress compression waves by applying the curl operator:

$$\rho\nabla \times \ddot{\mathbf{u}} = \nabla \times \nabla \cdot \boldsymbol{\sigma}. \tag{12}$$

For the acceleration terms on the left-hand side of Equation (10), we use the densities introduced in Biot's original theory[11]:

$$\rho_{11}\ddot{\mathbf{u}}^s + \rho_{12}\ddot{\mathbf{u}}^f = (1-f)\,\nabla \cdot \boldsymbol{\sigma}^s \tag{13a}$$

$$\rho_{12}\ddot{\mathbf{u}}^s + \rho_{22}\ddot{\mathbf{u}}^f = f\nabla\sigma^f \tag{13b}$$

with $\rho_{11} = (1-f)\,\rho^s - \rho_{12}$, $\rho_{22} = f\rho^f - \rho_{12}$, and coupling density $\rho_{12} < 0$. ρ^f and ρ^s are the densities of the fluid and the solid, respectively. The coupling density describes the transfer of shear motion between the compartments; since the fluid does not support shear motion itself, it acts as a parasitic mass that is "dragged along" by the solid, exerting a decelerating force which renders ρ_{12} negative.

Applying the curl operator to Equations (13a and 13b) yields the equations for the shear fields only, with $\mathbf{c} = \nabla \times \mathbf{u}$:

$$(1-f)\,\rho^s\ddot{\boldsymbol{c}}^s + \rho_{12}\left(\ddot{\boldsymbol{c}}^f - \ddot{\boldsymbol{c}}^s\right) = (1-f)\,\nabla \times \nabla \cdot \boldsymbol{\sigma}^s \tag{14a}$$

$$f\rho^f\ddot{\boldsymbol{c}}^f + \rho_{12}\left(\ddot{\boldsymbol{c}}^s - \ddot{\boldsymbol{c}}^f\right) = f\nabla \times \nabla\sigma^f = 0 \tag{14b}$$

In the second equation, we used the fact that $\nabla \times \nabla\xi = \mathrm{curl}\,\mathrm{grad}\xi = 0$ for any scalar field ξ. The second equation allows us to establish a relationship between the 2 shear displacement fields:

$$\ddot{\boldsymbol{c}}^f = -\frac{\rho_{12}}{f\rho^f - \rho_{12}}\ddot{\boldsymbol{c}}^s. \tag{15}$$

Since $\rho_{12} < 0$ and $f, \rho_f > 0$, the proportionality constant between $\ddot{\boldsymbol{c}}^f$ and $\ddot{\boldsymbol{c}}^s$ is real and positive. For oscillating displacements, $\tilde{\mathbf{c}} = \mathbf{c} \cdot e^{i(\omega t + \phi_0)}$, the 2 displacement fields can be expected to have approximately the same phase $\phi_0 + \omega t$.

3 | METHODS

Porosity estimation based on IR-MRI was developed and tested in two types of phantoms: one consisting of two separate liquid compartments of different T_1 relaxivity for emulating biphasic relaxation behavior, and the second phantom made of tofu for mimicking solid tissue with different porosities saturated by a fluid. For the in vivo part of the study, IR-MRI was used to determine porosity in the brains of 21 healthy volunteers (6 female and 15 male; mean age: 35 ± 10 years, age range: 23-58 years), and finally, IR-MRE was performed in seven volunteers (four female and three male; mean age: 33 ± 6 years, age range: 25-41 years). The study was approved by the institutional review board. All participants gave written informed consent.

3.1 | Fluid-fluid phantom

For the first experiment, a pair of saline solutions was prepared. Two 100-ml flat rectangular containers were filled with physiological saline solutions; one of them was doped with 10^{-4} mol/L gadolinium (Dotarem, Guerbet, Roissy, France) and attached to the other container to emulate 2 spatially separated fluid reservoirs of different T_1 relaxation times (see Figure 1).

3.2 | Solid-fluid phantoms

Eight tofu samples were produced in Plexiglas cylinders 5.6 cm in diameter, as described by Streitberger et al,[18] with different porosities by applying different amounts of pressure (Figure 2A). Reference porosities were determined after the IR-MRI experiments by measuring the drainable liquid volume. Due to water retention by surface adhesion, complete drainage of the free fluid would only have been

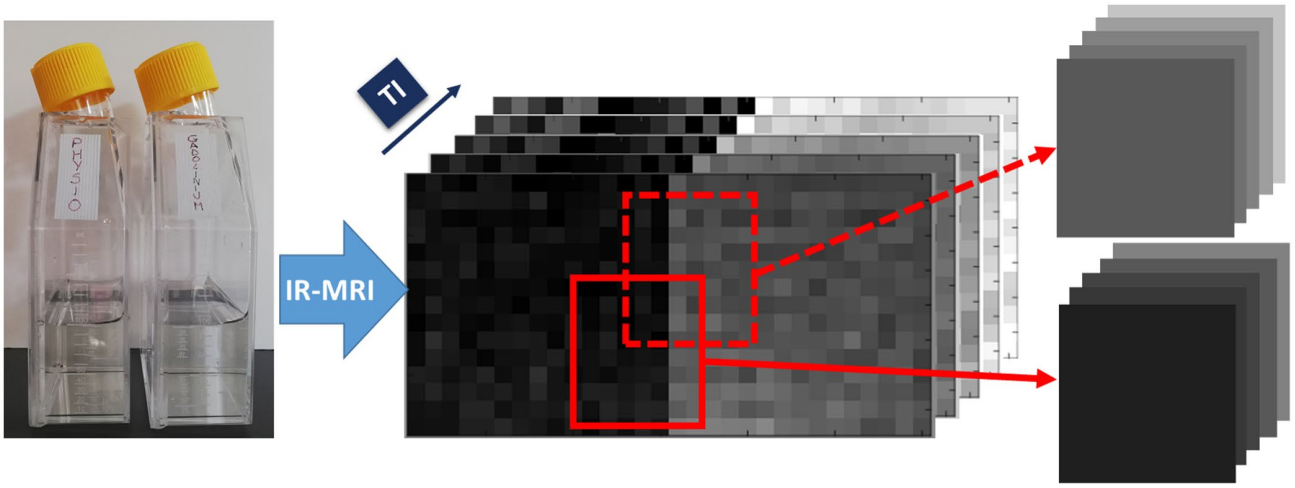

FIGURE 1 On the left, the two flat containers with the physiological solution and the gadolinium-doped solution are shown. After IR-MRI, ROIs were defined, including voxels from both fluids at different ratios at each TI to emulate supervoxels composed of the two media. The ratio at which voxels from both fluids are combined corresponds to the emulated porosity

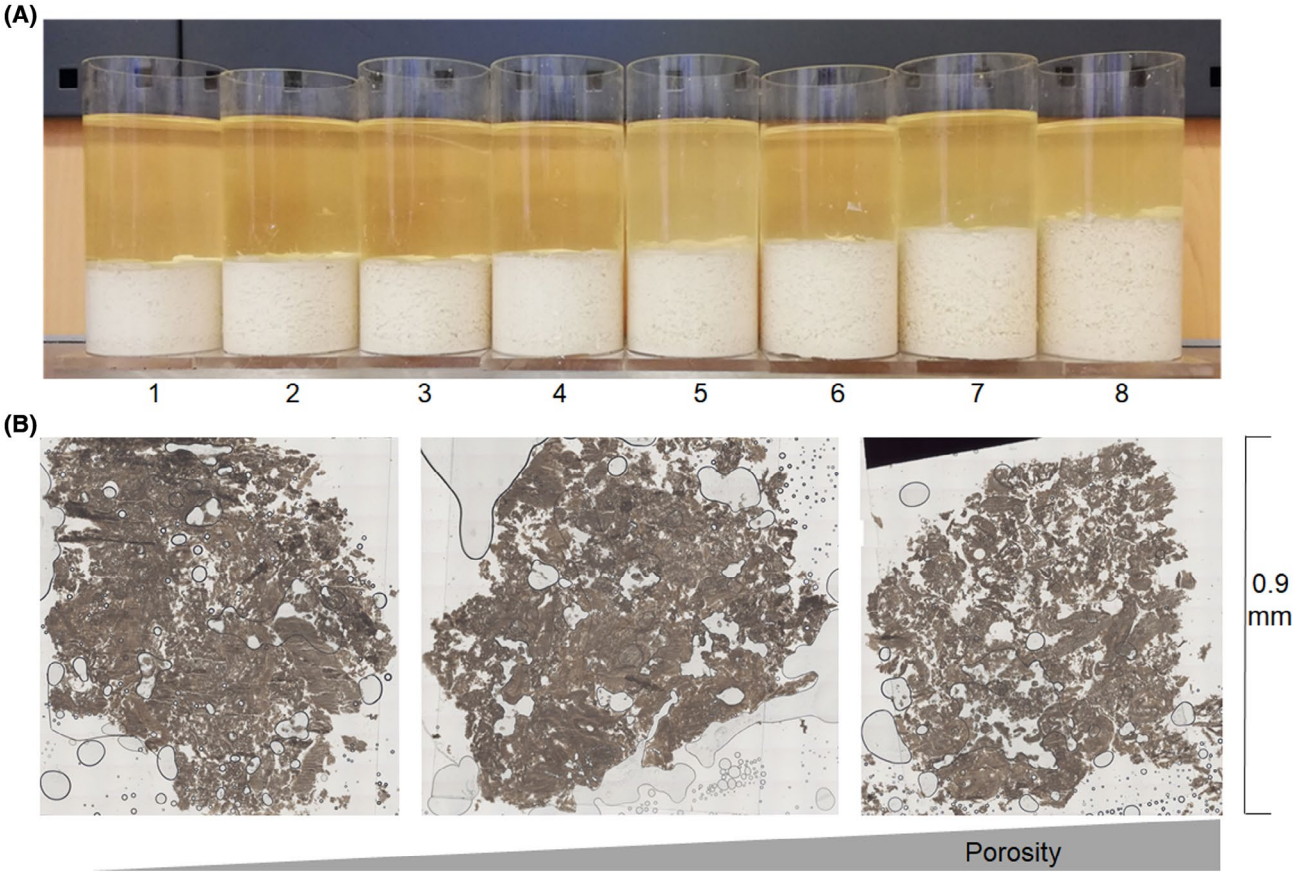

FIGURE 2 A, Eight tofu samples of increasing porosity from left to right. Remaining excess fluid above each tofu sample was used to quantify T_1 relaxation time of the pore fluid compartment. B, Three samples were extracted from the same tofu phantom to produce micrographs. The empty holes inside the sample are pores, in which the fluid compartment of the porous phantom can flow. The bubbles that appear in the images are attributable to the wet mount technique (Leica CV mount, Leica Biosystems, Richmond, USA), necessary to avoid shrinkage of the sample in contact with Kawamoto's adhesive tape. The micrographs show three different porosities, 0.11 ± 0.03, 0.13 ± 0.05, and 0.19 ± 0.04 (from left to right)

possible with excessively long drainage times, which in turn would have biased our results due to water evaporation or condensation. Therefore, we uniformly stopped the drainage after 10 min and extrapolated the experimentally quantified drainage rate to an infinite drainage time using a simple exponential decay model. Furthermore, an additional tofu sample was produced to evaluate the microscopic structure of the material. Cubes of approximately 1 cm^3 were excised from different locations in the tofu phantoms, fixed in paraformaldehyde, dehydrated in 20% sucrose solution for 48 h, and frozen in liquid nitrogen. Slices of 50 μm thickness were prepared according to Kawamoto's film method[19] using a cryostat (Leica CM 1850 UV, Nussloch, Germany), and light transmission microscopy (Figure 2B) was performed (Zeiss Axio Observer for Biology, Jena, Germany). From these micrographs, average porosity was calculated as the ratio of the pore area to the total area of the region of interest (ROI) after image segmentation.

Three additional tofu phantoms were similarly produced for the IR-MRI/IR-MRE experiments. In order to obtain larger phantoms, these were produced in cylindrical vessels with a diameter of 9.5 cm. For this purpose, the soy milk was first concentrated by evaporating a third of its volume before coagulation.

3.3 | IR-MRI/IR-MRE

All IR-MRI data were acquired with a single-shot spin-echo echo-planar imaging (EPI) sequence preceded by a slice-selective inversion pulse, preceded by a reference scan without inversion. The IR-MRI parameters used in the different experiments are compiled in Table 1. In the phantom studies, pauses were inserted between acquisitions to ensure that the effective TR was higher than $5 \cdot T_1^f$.

Additionally, in all in vivo IR-MRI experiments, T_1-weighted volumetric MRI was performed using an MP-RAGE (magnetization-prepared rapid gradient echo) sequence for anatomical reference.

For IR-MRI/IR-MRE experiments, IR-MRI was performed first at different TIs. Afterward, without moving the phantom or the volunteer, IR-MRE was performed twice, once without IR and second with a TI equal to the nulling TI of the fluid compartment. In the brain study, the fluid compartment was CSF, which was suppressed with TI = 2900 ms as priorly estimated from the relaxation measurement. The vibration frequency was 20 Hz and was induced using 2 pressurized air drivers placed side by side under the head and operated in opposed-phase mode.[20] Motion-encoding gradient (MEG) frequency was 39.53 Hz with 20 mT/m amplitude.

TABLE 1 Acquisition parameters used in the IR-MRI and IR-MRI/IR-MRE experiments

	Pure fluid phantom	Tofu phantom	In vivo brain imaging	Tofu phantom (for IR-MRI/MRE)	In vivo brain imaging (for IR-MRI/MRE)
MRI scanner	1.5T Siemens Sonata	1.5T Siemens Sonata	3T Siemens Trio	3T Siemens Prisma^{Fit}	3T Siemens Prisma^{Fit}
Coil	single-channel head coil	single-channel head coil	12-channel head coil	32-channel head coil	32-channel head coil
TE (ms)	36	35	45	65	65
TR (ms)	5150	6000	40550	17380	20000
Matrix size	32 × 88	112 × 32	100 × 100	108 × 110	108 × 110
Voxel volume (mm^3)	1.85 × 1.85 × 1.90	2 × 2 × 2	2 × 2 × 2	2 × 2 × 2	2 × 2 × 2
Slices	1	16	5	5	5
Interslice gap (mm)	–	2	2	2	2
TIs (ms)	120, 170, 220, 270, 320, 370, 420, 470, 520, 620, 720, 820, 920, 1020, 1220, 1420, 1620, 1820, 2020, 2220, 2420, 2620, 2820, 3020, 3400, 3800, 4200, 4600, 5000	120, 170, 220, 270, 320, 370, 420, 470, 520, 570, 620, 720, 820, 920, 1020, 1120, 1220, 1420, 1620, 1820, 2020, 2420, 2820, 3220, 3620	120, 250, 380, 510, 900, 1100, 1300, 1500, 1700, 1900, 2200, 2500, 2800, 3100, 3400, 3800, 4200, 4600, 5000	100, 200, 300, 400, 500, 600, 700, 800, 900, 1000, 1200, 1400, 1600, 1800, 2000, 2500, 3000, 3500, 4000, 5000	100, 200, 400, 600, 800, 1000, 1200,1600, 2000, 2500, 3000, 3500, 4000, 4500, 5000, 6000
Parallel imaging	–	–	Grappa factor 2	–	–

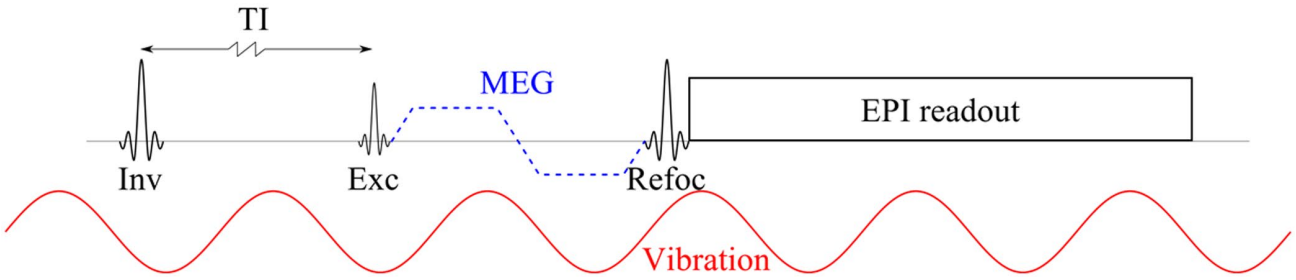

FIGURE 3 Sequence diagram of the acquisition of a single slice with the IR-MRI (black components) and IR-MRE (including MEG and vibration) protocol. The symbols denote: Inv: slice-selective inversion pulse; Exc: slice-selective 90° excitation pulse; Refoc: slice-selective 180° refocusing pulse; MEG: motion-encoding gradient (0th moment nulled, no flow compensation). The acquisition scheme is repeated identically for each slice of the imaging volume. The relative phase between the continuous vibration and the MEG was incremented in eight steps equally spaced over a full oscillation cycle, leading to a total of eight vibration phases × three MEG directions = 24 scans per slice for a single MRE acquisition. For IR-MRI, 16 to 29 scans were performed with different TIs to obtain a dense sampling of the relaxation curve. Two experiments were performed for IR-MRE: a reference scan without inversion pulse (corresponding to $TI = \infty$) and a second scan with TI for CSF-nulling

A diagram of the newly developed IR-MRE sequence is shown in Figure 3. The in vivo scanning session was supplemented by a T_1-weighted MP-RAGE sequence for segmentation. The total scan time per volunteer was approx. 30 min.

3.4 | Data processing

The "pure fluid" phantom data were processed in two steps: first, T_1 relaxation time, signal amplitude I, and noise offset C of each of the two fluids were obtained by fitting the monoexponential Equation (1) to the single-compartment IR-MRI signals within each of the two compartments. The signal of multiple ROIs, each containing voxels from both compartments at different ratios, was averaged into synthetic "supervoxels," emulating the biphasic signal from voxels with different porosities (see Figure 1). For consistency with theory, we refer to the saline solution with longer T_1 as the fluid and the Gd-doped solution with shorter T_1 as the solid. For each ROI, the fraction of voxels from the long-T_1 compartment in the ROI was taken as ground truth porosity. IR-MRI porosity of a biphasic supervoxel was derived by fitting either the full Equation (3) or reduced Equation (5) to the biexponential relaxation signal. As explained in the Theory section, T_1 and I values of the fluid compartment needed to be quantified separately and were used as input variables for our biphasic model to improve fitting stability. Consequently, T_1^f and I^f retrieved from the pure physiological saline solution were used as constants for the biphasic fit of either full Equation (3) or reduced Equation (5) in order to reconstruct T_1 times of the gadolinium-doped solution and porosities of the emulated supervoxels.

Solid-fluid tofu phantom data were analyzed by (1) fitting the IR-MRI signal decay of the excess fluid on top of the phantom with a monophasic model (Equation 1) in order to extract T_1^f and I^f and (2) using these parameters as constants for the biexponential fits (Equation 5) of the biphasic tofu IR-MRI signal.

The same strategy was applied to in vivo IR-MRI data by treating CSF properties as dominating fluid properties of brain tissue. Hence, the IR-MRI signal of CSF in the lateral ventricles was (1) analyzed by monoexponential fitting (Equation 1) for determination of T_1^f and I^f and (2) using these values as constants for fitting the biexponential signal relaxation of the IR-MRI (Equation 5) was applied to the brain data on a voxel-by-voxel basis.

In the IR-MRI/IR-MRE experiments, the IR-MRI scans were processed in the same way as in the previous IR-MRI experiment to obtain f and T_1^s maps aligned with the IR-MRE scans. Equation (8) was solved to obtain the displacement field of the fluid compartment. The fluid compartment being present at a lower quantity than the solid, its relative displacement field is more sensitive to noise than the solid compartment. Therefore, it was then filtered with a Butterworth low-pass filter with a cutoff of 50 m^{-1} and order 1. The curl of the fluid and solid displacement fields was calculated using central differences for interior data points and single-sided differences at the end points. Afterward, ρ_{12} was estimated by solving Equation (15). We assumed $\rho^f = 1000$ kg/m^3, equal to the density of water.

3.5 | Statistical analysis

In the IR-MRI in vivo experiments, for generating tissue probability maps of gray matter (GM), white matter (WM), and CSF, IR-MRI scans were co-registered to MP-RAGE images using Statistical Parametric Mapping (SPM) 12 software (The Wellcome Centre for Human Neuroimaging, London, UK) and segmented using the extended version of the unified segmentation routine.[21] Porosity maps and T_1 maps were segmented based on SPM-generated probability maps. A voxel was assigned to a compartment if its probability value for that compartment exceeded 80%. Group mean values and SDs of CSF T_1 and monophasic T_1, compartmental T_1, and porosity

of GM and WM were calculated. A paired *t*-test analysis was performed for average porosity and normalized solid T_1 values of WM and GM in each volunteer. Statistical tests were performed in Matlab (Mathwork Inc., Natick, USA, version 2018), discarding all values for which the coefficient of determination, R^2, of the fitting was lower than 0.9.

In the IR-MRE phantom and in vivo experiments, the magnitude and oscillation phase of the curl components after Fourier transform were analyzed separately. A right-tailed *t*-test was used to test if the magnitude of the solid curl component was higher than the amplitude of the fluid component, as predicted by theory. To test the assumption that solid and fluid oscillate in phase, as predicted by theory (Equation 15), the motion phase from one compartment was plotted versus that of the other on a per-voxel basis, and linear regression was calculated for each sample and each volunteer. Due to the instabilities caused by the denominator of the rearranged Equation (15), $\rho_{12} = \frac{f\rho^f \ddot{c}^f}{\ddot{c}^f - \ddot{c}^s}$, voxels with $|\ddot{c}^s| < 5 \cdot 10^{-4}$ were removed from the statistical analysis. Statistical significance was assumed for $P < .05$. Median and interquartile intervals were estimated for each tofu sample and in the in vivo brain for WM and GM separately.

4 | RESULTS

4.1 | Fluid-fluid phantom

Figure 4 displays IR-MRI results obtained in the fluid-fluid phantom obtained with the full model (Equation 3) and the reduced model (Equation 5). Error bars indicate that the SE of estimated parameters is smaller for the reduced Equation

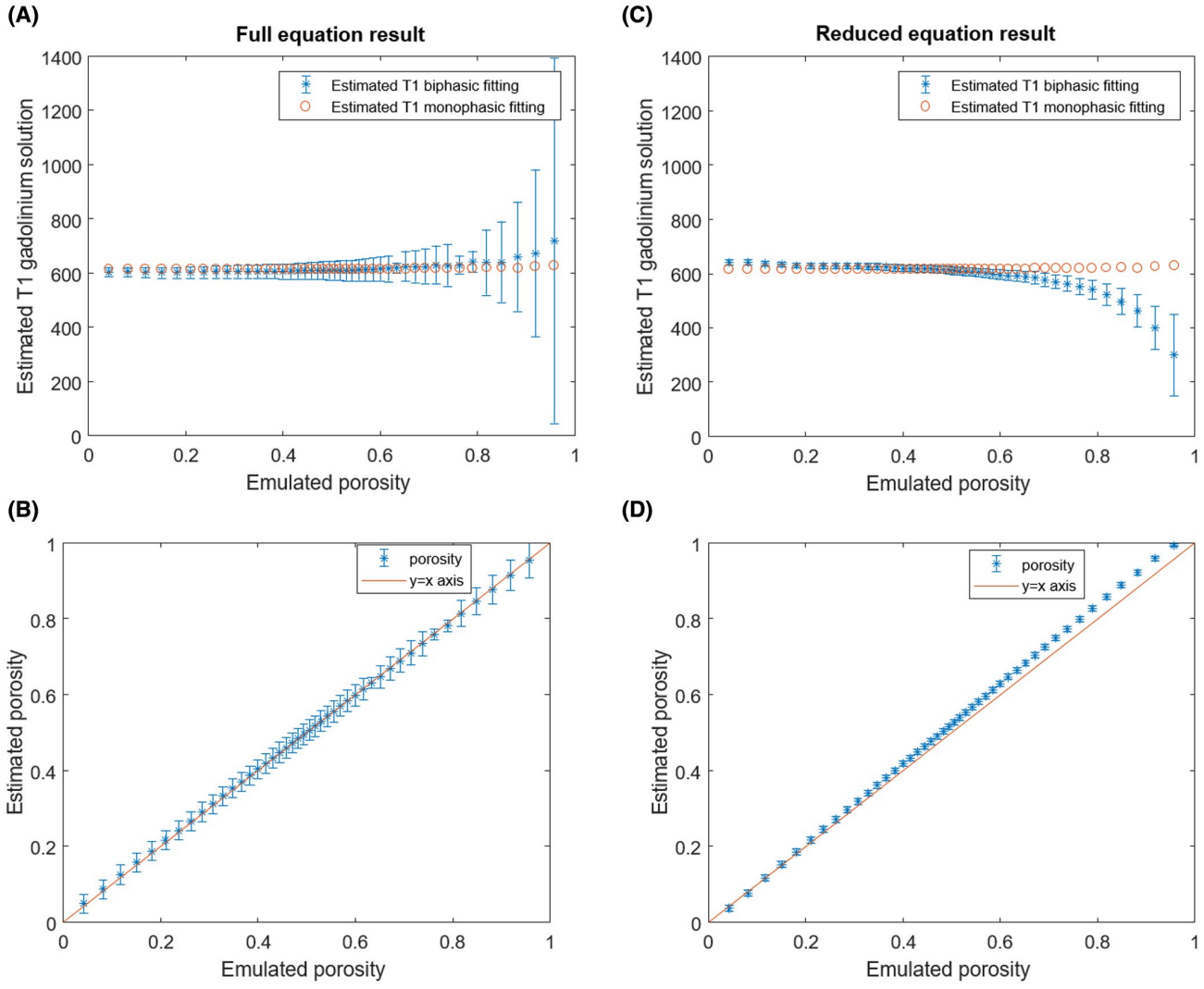

FIGURE 4 A, Comparison of T_1 of the gadolinium solution obtained by fitting the full biphasic model (Equation 3) to the supervoxel data and T_1 of the same solution obtained by fitting the monophasic model (Equation 1) only to the voxels of the doped solution contained in the same supervoxel. B, Comparison of IR-MRI-derived porosity obtained with the full model (Equation 3) and emulated porosity. C and D, Same analysis as A/B, but for data obtained with the reduced model (Equation 5). In each figure, the error bars represent the SE of estimation of the evaluated parameter

(5) (mean SE of f: ±0.007, of T_1^s: ±22 ms) than for the full Equation (3) (mean of f: ±0.03, of T_1^s: ±63 ms). However, Equation (5) tends to underestimate T_1^s and to overestimate porosity at higher ground truth porosities. For example, at ground truth porosities $f > 0.8$, we identified an overestimation of f on the order of 4% and of T_1^s on the order of 3%. Nevertheless, porosities reconstructed using the reduced Equation (5) were in excellent agreement with ground truth ($R = 1$, $P = 0$, mean residual error of porosity: ±0.02).

4.2 | Solid-fluid phantoms IR-MRI

The porous nature of the solid-fluid phantoms was confirmed by microscopy images, as shown in Figure 2B. Porosities in different regions quantified by image analysis were 0.11 ± 0.03, 0.13 ± 0.05, and 0.19 ± 0.04, indicating an inhomogeneous porous structure across macroscopic distances (Supporting Information Figure S1, which is available online).

Figure 5A shows porosity maps of the central slice of each tofu sample reconstructed from IR-MRI using Equation (5). Mean porosities ranged from 0.12 to 0.27. Porosity determined by draining tofu samples ranged from 0.08 to 0.30, indicating good agreement of IR-MRI with reference porosity values. Figure 5B presents spatially averaged IR-MRI porosity values versus draining porosity. The error bars of the IR-MRI porosity data represent the SD of porosity across slices, while the error bars of the draining porosity data correspond to the measurement error. IR-MRI porosity is correlated with draining porosity ($R = 0.99$, $P < 10^{-5}$). Because water adhesion causes retention of some of the free water in the tofu, draining porosity is prone to underestimation in tofu, especially at low porosities.

4.3 | In vivo brain study IR-MRI

Figure 6 shows IR-MRI porosity and solid-tissue T_1 of in vivo brain. Average CSF T_1 across all volunteers was 4257 ± 157 ms, while T_1^s and f were 1172 ± 36 ms and 0.14 ± 0.02 in GM and 800 ± 15 ms and 0.05 ± 0.01 in WM, respectively. These parameters were statistically significantly different between GM and WM (all $P < 10^{-16}$). Nevertheless, porosity and T_1^s represent independent information, as demonstrated by the histograms shown in Figure 7. These plots illustrate that T_1^s values are distributed with 2 distinct peaks corresponding to GM and WM, whereas porosity displays a more continuous single-peaked and wider distribution.

4.4 | Solid-fluid phantoms IR-MRI/IR-MRE

As shown in Figure 8A, the average shear wave amplitude in the solid is higher than in the fluid ($P < .05$). Voxel-by-voxel linear fitting of the phases of $\boldsymbol{c}^f$ and $\boldsymbol{c}^s$ resulted in

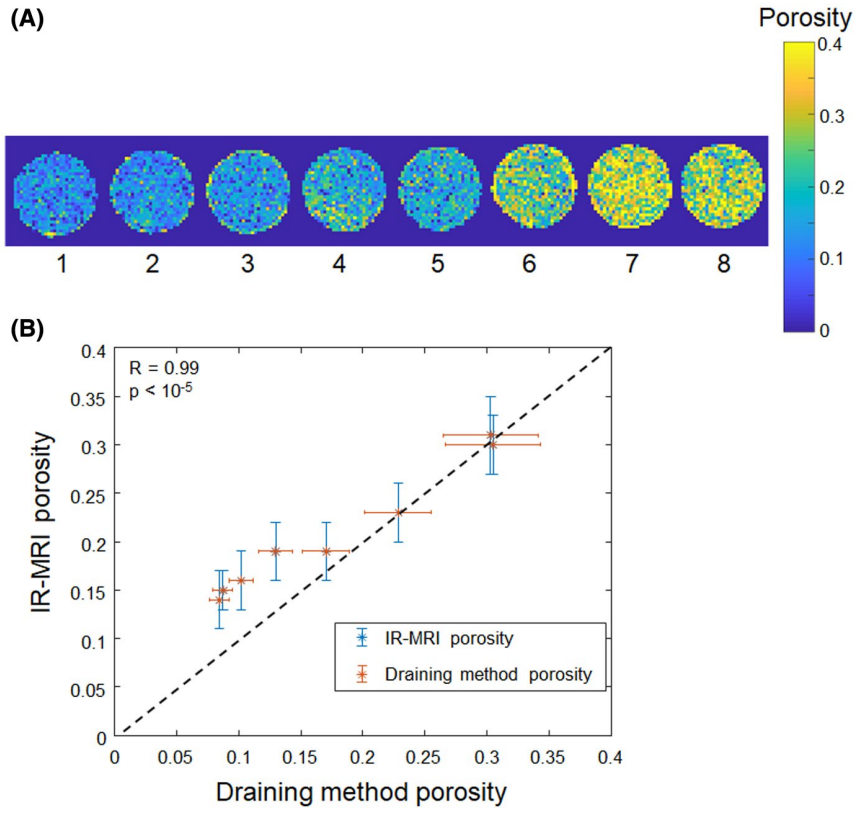

FIGURE 5 A, Porosity maps of the central slice of each of the eight tofu samples shown in Figure 1. B, IR-MRI-derived porosity plotted versus the porosity obtained by draining the fluid compartment from the samples. The black dashed line represents perfect agreement of the two methods. The error bars for IR-MRI porosity represent the SD of interslice average porosity, while the error bars for draining porosity represent the measurement error of the tofu and drained fluid volumes, propagated to the porosity value

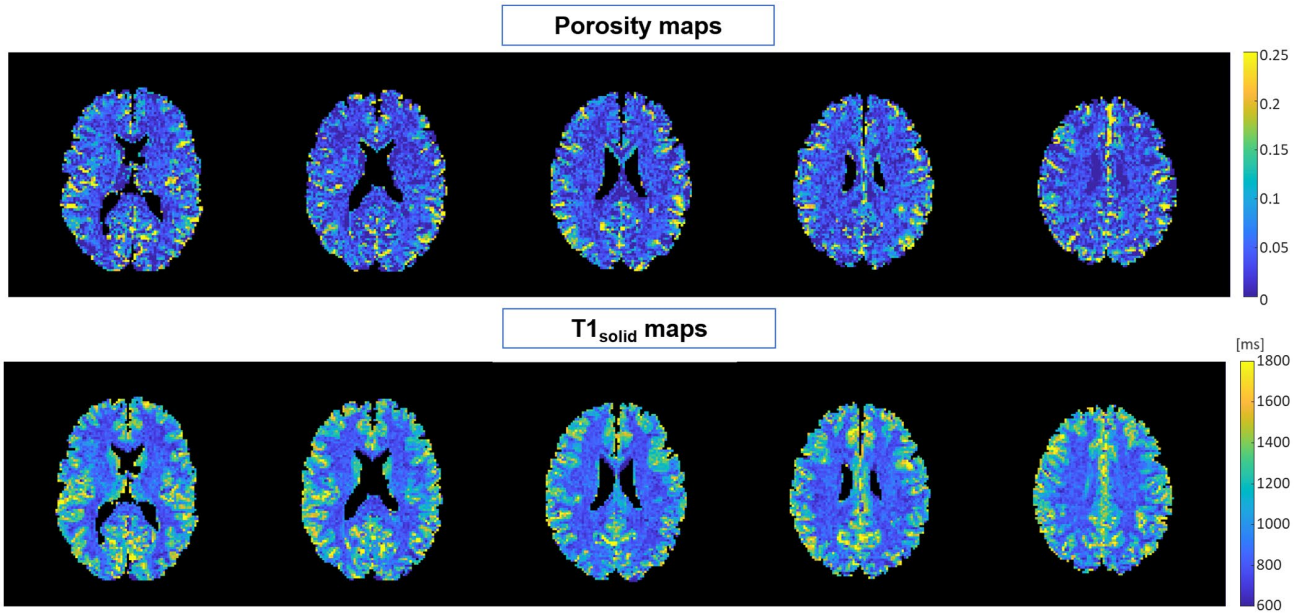

FIGURE 6 Porosity maps (top row) and T_1^s maps (bottom row) of five slices from one volunteer. In both sets of slices, CSF-filled regions, such as the ventricles, are excluded from analysis. As discussed for the liquid-liquid phantom, biphasic fitting reliability is not optimal in areas with porosity >0.5

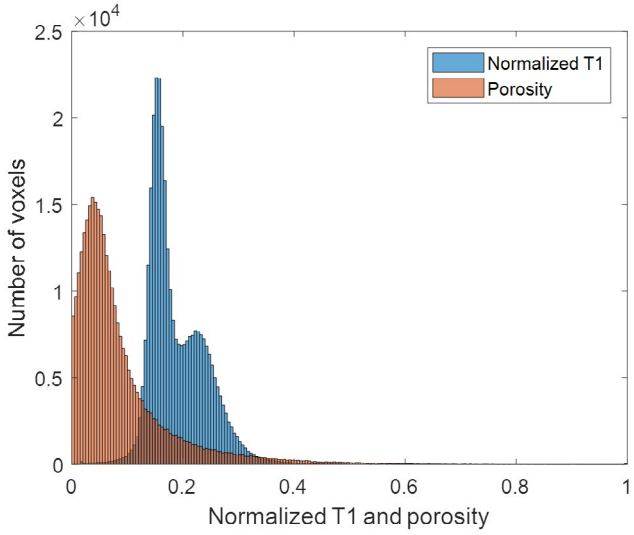

FIGURE 7 Histograms of normalized T_1 and porosity of the brain pooled across all volunteers. T_1 values were rescaled between 0 and 1. The two distributions are clearly different: porosity shows only one peak, while T_1^s reveals two distinct peaks that coincide with mean T_1^s values in GM and WM

an average slope of 0.93 ± 0.07, offset of 0.10 ± 0.01, and R^2 = 0.90 ± 0.07. As an example, the phase data fitting obtained from the same sample as in Figure 8A is shown in Figure 8B. Maps of ρ_{12} were produced for each slice (Figure 8A). The distribution of ρ_{12} is strongly asymmetrical (Supporting Information Figure S2), therefore median and interquartile range were calculated and resulted in −114 (−318, −24) kg/m^3, −117 (−330, −21) kg/m^3, and −190 (−511, −22) kg/m^3 for the three tofu phantoms.

4.5 | In vivo brain study IR-MRI/MRE

Figure 9A shows the curl of the solid and fluid. The average shear wave amplitude in the solid is higher than in the fluid in each volunteer ($P < .05$). Voxel-by-voxel linear fitting of the phases of $\ddot{\boldsymbol{c}}^f$ and $\ddot{\boldsymbol{c}}^s$ resulted in an average slope of 0.98 ± 0.01, offset of −0.01 ± 0.09, and R^2 = 0.95 ± 0.02. As an example, the phase data fitting obtained from the same volunteer as in Figure 9A is shown in Figure 9B. Maps of ρ_{12} were produced for each slice (Figure 9A), and group average medians of −22 ± 29 kg/m^3 and −38 ± 4 kg/m^3 were obtained for GM and WM, respectively.

5 | DISCUSSION

In this study, we introduced an in vivo porosity quantification technique based on T_1 relaxation measurement combined with MRE to separate solid and fluid displacement fields and to estimate dynamic coupling density.

The fluid-fluid phantom experiment served as a first validation of porosity estimation in a highly simplified setting. It incorporated biexponential fitting with four variables and resulted in stable values over a wide range of porosities ($f < 0.9$). Furthermore, it was shown that the simplified model (Equation 5) with only three free parameters produced

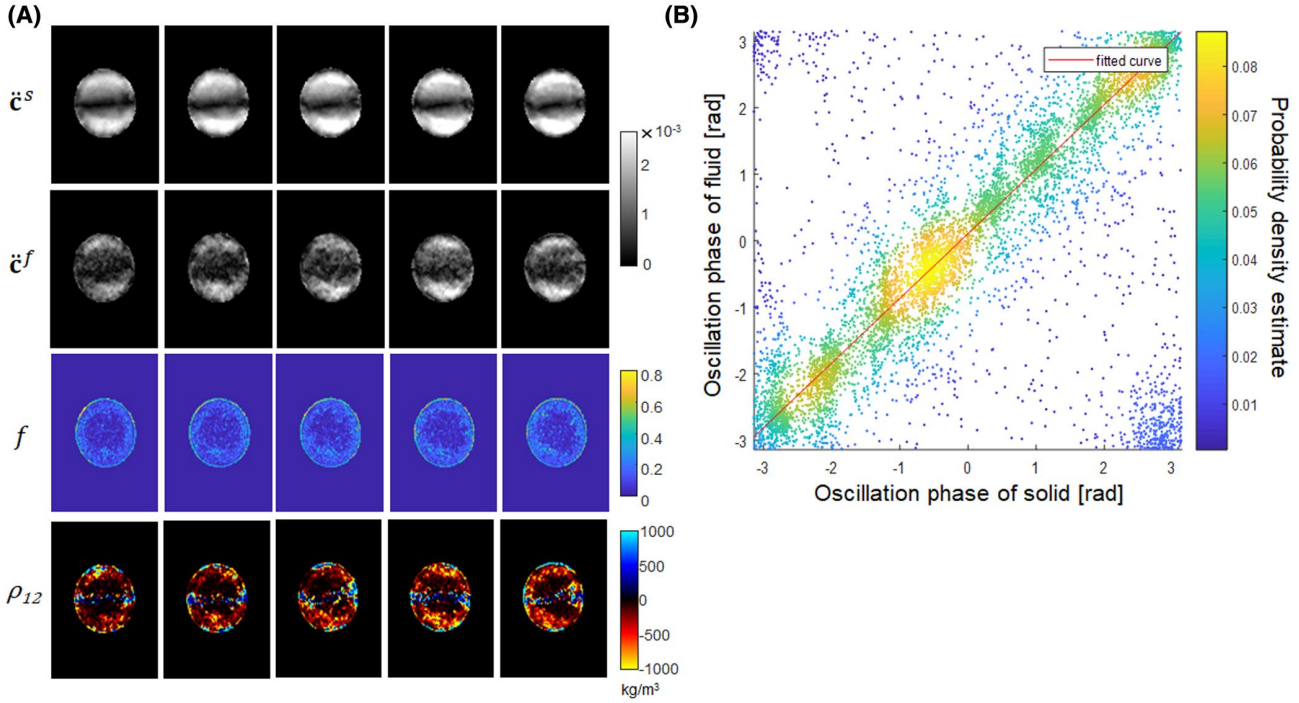

FIGURE 8 A, Magnitude of the through-plane component of the curl of the solid compartment (first row) and fluid compartment (second row) of a tofu sample. The curl of the solid compartment shows higher values than that of the fluid compartment. Porosity maps (third row) and corresponding ρ_{12} maps. B, Voxel-by-voxel plot of the fluid and solid curl phase. The color map represents the probability density estimate of the points in the plot, and the red line represents the linear regression of the plotted data. Due to phase circularity along both axes, the wrapped data points in the top left and bottom right corners cannot be unwrapped unambiguously. However, their effect on linear regression was found to be negligible

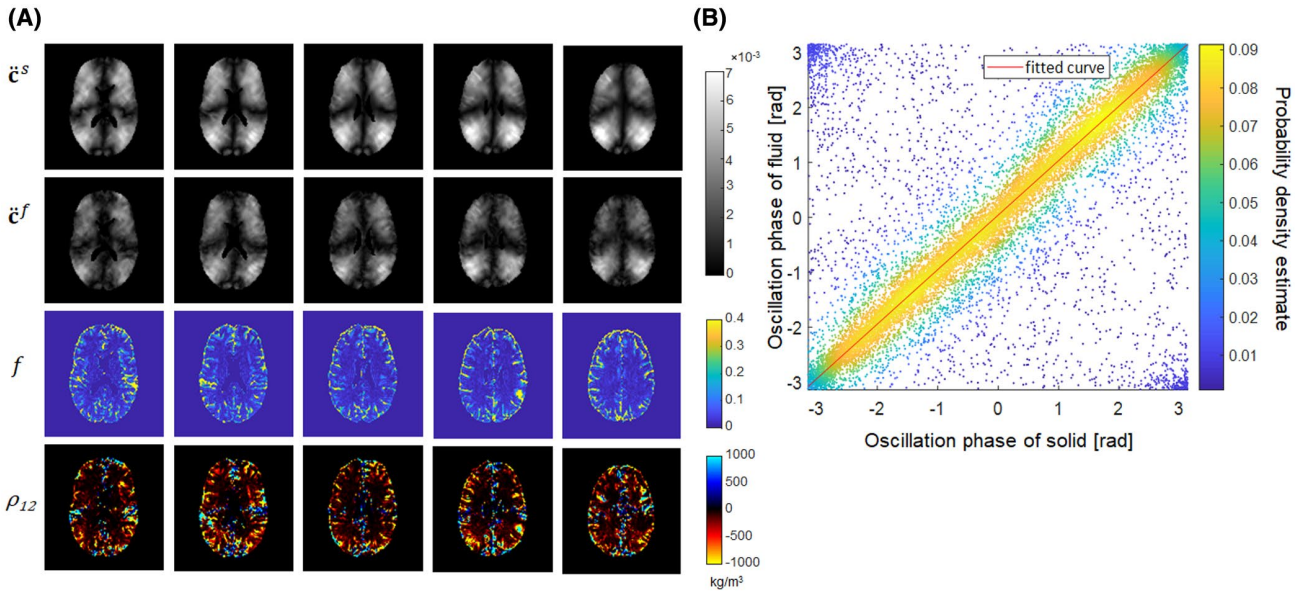

FIGURE 9 A, Magnitude of the through-plane component of the curl of the solid compartment (first row) and fluid compartment (second row). Furthermore, porosity map, and corresponding ρ_{12} maps of a healthy volunteer are shown. B, Voxel-by-voxel plot of the phase of the fluid and solid curl in the same healthy volunteer shown in Figure 8

comparable results within a more constrained range of porosities ($f < 0.5$). However, most biological soft tissues have porosities below the threshold of 0.5: for example, previous studies have shown that average liver tissue porosity is 14%[22], while brain extracellular space (ECS), which contains the fluid volumes quantified by our IR-MRI method, has a

porosity on the order of 20%.[15] Since this is clearly below 50%, we consider the simplified model of Equation (5) valid for IR-MRI reconstruction.

The solid-fluid phantom made of tofu allowed us to validate our method in a biphasic soft-tissue-mimicking material. As with biological tissues, the assumption that tofu, with its composition of an interspersed aqueous solvent and coagulated proteins, can be separated into two distinct compartments is an oversimplification. Furthermore, as revealed by microscopy, the heterogeneity of pores in tofu on the millimeter scale imposes challenges in defining ground truth porosity. Our method for quantifying drainage velocity in conjunction with exponential extrapolation improved the estimation of reference porosity and was more consistent than other methods, including microscopic analysis (Supporting Information S1) or measurement of the fluid volume drained after a fixed drainage time. Nevertheless, there is an offset between draining porosity and IR-MRI, which we attribute to water adhesion at polar groups of the coagulated soy proteins, which in turn leads to retention of aqueous solvent within the solid tissue matrix. Albeit not accessible by drainage, such compartments of retained fluid might still contribute to IR-MRI-derived porosity, while resulting in an overall underestimation of draining porosity.

The biphasic equation (Equation 5) collapses in the quasi-monophasic edge cases $f \to 0$ and $f \to 1$. Therefore, we excluded the ventricles and voxels with $f < 10^{-4}$ from further analysis. Overall, 0.5% of voxels were discarded because of unreliable fitting ($R^2 < 0.9$), and an additional 16.8% of the remaining voxels were discarded based on the $f < 10^{-4}$ criterion.

In the brain, magnetization transfer (MT) effects have to be considered that can interfere with T_1 relaxation measurements.[23,24] To assess the potential effect of MT on porosity estimation, we performed an additional experiment in three healthy volunteers in which we compared the standard IR-MRI protocol, as described above, with a modified version of the protocol with only two slices and excessively long idle time (60 s) between slice acquisitions to allow for complete relaxation between excitations. This experiment revealed that the difference between these 2 scans caused an uncertainty in the porosity estimation of $(17 \pm 14)\cdot 10^{-3}$, $(43 \pm 15)\cdot 10^{-3}$, and $(44 \pm 35)\cdot 10^{-3}$ in homogeneous WM regions for the three subjects. We conclude that, while MT does have an effect on porosity quantification, it does not limit the general applicability of the proposed method (Supporting Information Figure S3). Nevertheless, a sequence optimized to minimize MT would potentially improve the accuracy of the method.

The histograms of T_1 and porosity, as shown in Figure 7, with a single peak in the porosity data and two peaks for T_1, indicate that there is no monotonous mapping between these two quantities, that is, they can be considered to represent unrelated information. Naturally, the type of fluid depends on the specific type of tissue under investigation. In brain tissue, ECS mainly contains a fluid similar in composition to CSF.[25] Several studies have determined the ECS volume fraction[26-28] reporting values between 15% in WM and 30% in GM of in vivo rat brain.[15] In contrast, the vascular volume in the brain does not exceed 3% in GM and 1.5% in WM.[29] As a consequence, blood, with its significantly shorter T_1 than CSF, as well as other short-T_1 liquids, will at least partially be classified as belonging to the solid compartment, thus leading to systematic underestimation of total porosity. In addition to blood, bound water within the ECS which cannot freely move and, thus, exhibits much shorter T_1-times than free CSF, can be considered as part of the solid matrix, both for T_1-relaxation times and mechanically As a result, brain porosity measured by our IR-MRI method is lower than the values reported in the aforementioned studies and should rather be interpreted as CSF porosity.

The shear wave amplitude of the fluid is significantly lower than that of the solid, in both tofu and brain. As predicted by theory, the phases of fluid and solid motion were correlated, indicating in-phase oscillation of the two compartments at different amplitudes. The ρ_{12} maps are encouraging, as they show negative values in agreement with the theory, except for regions of zero deflection amplitudes (e.g., in the vicinity of standing wave nodes), making the difference between curl components in Equation (15) prone to sign errors, as shown in Figures 8A and 9A (Supporting Information Figure S4). The higher SD in GM is a consequence of many voxels near the segmented CSF with porosities higher than 0.5, which, as discussed, lead to an unstable estimation. Knowledge of compartmental displacement fields is a major step toward the full exploitation of the poroelastic medium model in the context of MRE, which has been previously supported by parameter assumptions[3] or an effective medium approach.[9] Separation of the displacement fields could contribute to the further advancement of elastography and poroelastography of hydrocephalus[30-32] and, thus, help in further elucidating the development of the disease and improving its diagnosis. Our results could also contribute to a deeper understanding of brain tumors, especially glioblastoma and meningioma, whose "anomalous" mechanical behavior has been detected by brain elastography.[18]

Our study has a few limitations. First, our model is biphasic and homogeneous in each voxel with respect to the MRI signal, assuming a sharp peak in the relaxation time spectrum of each compartment. This assumption ignores proton exchange across interfaces between different pools of protons,[33] magnetization transfer, the widening of the peaks based on proton interactions, and continuous T_1 spectra. Second, inversion of the biexponential model is ill-conditioned when porosity approaches the limits of 0 or 1, which is not an issue in typical biological soft tissues as long as fluid-filled spaces are excluded from porosity analysis. Finally, possible slight

movement of volunteers can cause a spatial mismatch between the inverted and non-inverted MRE scans, requiring additional alignment steps.[34] In this work, the volunteers' head position was fixed with thick cushions to minimize head motion.

6 | CONCLUSIONS

We have demonstrated for the first time that the combination of IR-MRI and IR-MRE in conjunction with specialized data processing techniques can successfully disentangle externally induced fluid and solid displacement fields in the in vivo human brain. IR-MRI allowed quantification of brain tissue porosity based on simplification of highly complex fluid-solid interactions in biological tissues. Porosity, which reflects the fluid-volume fraction of the human brain, was inferred from a biphasic model, and validation was supported by microscopic and drainage-based analysis in tofu phantoms. Reconstructed coupling density values are negative in both phantoms and in vivo brain, in agreement with theory. Our findings are intended to inspire future studies of soft tissues, which can be successfully modeled as poroelastic media, and to propose a new method for evaluating the interaction of the two constituent compartments.

ACKNOWLEDGMENTS

The authors gratefully acknowledge support from the German Research Foundation (GRK2260 BIOQIC, SFB1340 Matrix in Vision). We thank Helena Radbruch, M.D., and Angela Ariza de Schellenberger, Ph.D., for their valuable help in the fields of histology and microscopy. Open access funding enabled and organized by Projekt DEAL.

ORCID

Ledia Lilaj https://orcid.org/0000-0001-8222-0397
Jürgen Braun https://orcid.org/0000-0001-5183-7546
Ingolf Sack https://orcid.org/0000-0003-2460-1444
Sebastian Hirsch https://orcid.org/0000-0001-8187-8242

REFERENCES

1. Muthupillai R, Lomas DJ, Rossman PJ, Greenleaf JF, Manduca A, Ehman RL. Magnetic resonance elastography by direct visualization of propagating acoustic strain waves. *Science*. 1995;269:1854-1857.
2. Franceschini G, Bigoni D, Regitnig P, Holzapfel GA. Brain tissue deforms similarly to filled elastomers and follows consolidation theory. *J Mech Phys Solids*. 2006;54:2592-2620.
3. Mcgarry MDJ, Johnson CL, Sutton BP, et al. Suitability of poroelastic and viscoelastic mechanical models for high and low frequency MR elastography. *Med Phys*. 2015;42:947-957.
4. Armstrong CG, Mow VC. An analysis of the unconfined compression of articular cartilage. *J Biomech Eng*. 1984;106:165-173.
5. Fortin M, Buschmann MD, Bertrand MJ, Foster FS, Ophir J. Dynamic measurement of internal solid displacement in articular cartilage using ultrasound backscatter. *J Biomech*. 2003;36:443-447.
6. Righetti R, Garra BS, Mobbs LM. The feasibility of using poroelastographic techniques for distinguishing between normal and lymphedematous tissues in vivo. *Phys Med Biol*. 2007;52:6525.
7. Biot MA. General theory of three-dimensional consolidation. *J Appl Phys*. 1941;12:155-164.
8. Mcgarry M, Van Houten E, Solamen L, Gordon-Wylie S, Weaver J, Paulsen KD. Uniqueness of poroelastic and viscoelastic nonlinear inversion MR elastography at low frequencies. *Phys Med Biol*. 2019;64:075006.
9. Hirsch S, Klatt D, Freimann F, Scheel M, Braun J, Sack I. In vivo measurement of volumetric strain in the human brain induced by arterial pulsation and harmonic waves. *Magn Reson Med*. 2013;70:671-683.
10. Tan L, McGarry MDJ, Van Houten EEW, et al. A numerical framework for interstitial fluid pressure imaging in poroelastic MRE. *PLoS One*. 2017;12:e0178521.
11. Biot MA. Theory of propagation of elastic waves in a fluid-saturated porous solid. II. Higher frequency range. *J Acoust Soc Am*. 1956;28:179-191.
12. Aguilera JM, Stanley DW. *Microstructural Principles of Food Processing and Engineering*. Gaithersburg, Maryland: Aspen Publishers, Inc; 1999.
13. Sack I, Schaeffter T. *Quantification of Biophysical Parameters in Medical Imaging*. Cham, Switzerland: Springer; 2018.
14. Nagashima T, Tamaki N, Matsumoto S, Horwitz B, Seguchi Y. Biomechanics of hydrocephalus: A new theoretical model. *Neurosurgery*. 1987;21:898-904.
15. Syková E, Nicholson C. Diffusion in brain extracellular space. *Physiol Rev*. 2008;88:1277-1340.
16. Parker KJ. A microchannel flow model for soft tissue elasticity. *Phys Med Biol*. 2014;59:4443-4457.
17. Parker KJ. Experimental evaluations of the microchannel flow model. *Phys Med Biol*. 2015;60:4227-4242.
18. Streitberger K, Lilaj L, Schrank F, et al. How tissue fluidity influences brain tumor progression. *Proc Natl Acad Sci USA*. 2020;117:128-134.
19. Kawamoto T. Use of a new adhesive film for the preparation of multi-purpose fresh-frozen sections from hard tissues, whole-animals, insects and plants. *Arch Histol Cytol*. 2003;66:123-143.
20. Dittmann F, Tzschätzsch H, Hirsch S, et al. Tomoelastography of the abdomen: Tissue mechanical properties of the liver, spleen, kidney, and pancreas from single MR elastography scans at different hydration states. *Magn Reson Med*. 2017;78:976-983.
21. Ashburner J, Friston KJ. Friston KJ. Unified segmentation. *Neuroimage*. 2005;26:839-851.
22. Debbaut C, Vierendeels J, Casteleyn C, et al. Perfusion characteristics of the human hepatic microcirculation based on three-dimensional reconstructions and computational fluid dynamic analysis. *J Biomech Eng*. 2012;134:011003.
23. Wolff S, Balaban RS. Magnetization transfer contrast (MTC) and tissue water proton relaxation in vivo. *Magn Reson Med*. 1989;10:135-144.
24. Dixon WT, Engels H, Castillo M, Sardashti M. Incidental magnetization transfer contrast in standard multislice imaging. *Magn Reson Imaging*. 1990;8:417-422.

25. Kamali-Zare P, Nicholson C. Brain extracellular space: geometry, matrix and physiological importance. *Basic Clin Neurosci*. 2013;4:282-286.
26. Van Harreveld A, Crowell J, Malhotra SK. A study of extracellular space in central nervous tissue by freeze-substitution. *J Cell Biol*. 1965;25:117-137.
27. Van Harreveld A. The extracellular space in the vertebrate central nervous system. In: Bourne GH, ed. *The Structure and Function of Nervous Tissue 4*. New York: Academic Press, Inc; 1972: 447-511.
28. Ohno N, Terada N, Saitoh S, Ohno S. Extracellular space in mouse cerebellar cortex revealed by in vivo cryotechnique. *Comp Gen Pharmacol*. 2007;505:292-301.
29. Schlageter KE, Molnar P, Lapin GD, Groothuis DR. Microvessel organization and structure in experimental brain tumors: Microvessel populations with distinctive structural and functional properties. *Microvasc Res*. 1999;58:312-328.
30. Streitberger K, Wiener E, Hoffmann J, et al. In vivo viscoelastic properties of the brain in normal pressure hydrocephalus. *NMR Biomed*. 2011;24:385-392.
31. Perriñez PR, Pattison AJ, Kennedy FE, Weaver JB, Paulsen KD. Contrast detection in fluid-saturated media with magnetic resonance poroelastography. *Med Phys*. 2010;37:3518-3526.
32. Pattison AJ, Perrinez PR, Mcgarry M, Weaver JB, Paulsen KD. Feasibility study to measure changes in intracranial pressure using magnetic resonance poroelastography. In Proceedings of the 10th Annual Meeting of ISMRM, Stockholm, Sweden, 2010, p. 3406.
33. Deoni SCL, Rutt BK, Jones DK. Investigating the effect of exchange and multicomponent T1 relaxation on the short repetition time spoiled steady-state signal and the DESPOT1 T1 quantification method. *Magn Reson Med*. 2007;25:570-578.
34. Fehlner A, Hirsch S, Weygandt M, et al. Increasing the spatial resolution and sensitivity of magnetic resonance elastography by correcting for subject motion and susceptibility-induced image distortions. *J Magn Reson Imaging*. 2017;46:134-141.

SUPPORTING INFORMATION

Additional Supporting Information may be found online in the Supporting Information section.

FIGURE S1 Average IR-MRI porosity of 4 samples compared to the corresponding porosity measured by the microscopy
FIGURE S2 Histogram of the distribution of ρ_{12} values in the tofu phantom represented in Figure 8
FIGURE S3 Comparison of porosity in homogenous areas of WM obtained by analyzing standard IR-MRI scans and long idle time IR-MRI scans
FIGURE S4 Comparison between the anatomical scans and ρ_{12} maps shown in Figure 9

How to cite this article: Lilaj L, Fischer T, Guo J, Braun J, Sack I, Hirsch S. Separation of fluid and solid shear wave fields and quantification of coupling density by magnetic resonance poroelastography. *Magn Reson Med*. 2021;85:1655–1668. https://doi.org/10.1002/mrm.28507